

Quantum oscillations and transport evidence of topological bands in La_3MgBi_5 single crystals


Xin Han (韩鑫)^{1,2,*} Hanqi Pi (皮涵琦)^{1,3,*} Dayu Yan (闫大禹)^{1,*} Ruihan Zhang (张锐涵)^{1,3} Yong Li (李勇)^{1,2}
 Xiang Wang (王翔)^{1,3} Zhiling Dun (顿志凌)^{1,†} Zhijun Wang (王志俊)^{1,3} Hai L. Feng (冯海)^{1,‡}
 Quansheng Wu (吴泉生)^{1,3,§} and Youguo Shi (石友国)^{1,2,3,4,||}

¹Beijing National Laboratory for condensed Matter Physics and Institute of Physics, Chinese Academy of Sciences, Beijing 100190, China

²Center of Materials Science and Optoelectronics Engineering, University of Chinese Academy of Sciences, Beijing 100190, China

³School of Physical Sciences, University of Chinese Academy of Sciences, Beijing 100190, China

⁴Songshan Lake Materials Laboratory, Dongguan, Guangdong 523808, China

 (Received 23 December 2022; revised 19 April 2023; accepted 4 August 2023; published 24 August 2023)

In this work, we synthesized single crystals of La_3MgBi_5 and systematically investigated their structure, magnetism, and transport properties. La_3MgBi_5 belongs to the A_3MX_5 family ($A = \text{Ca-Ba}$ or rare earth, $M =$ transition materials or Mg, $X =$ chalcogen or pnictogen) and has a quasi-one-dimensional structure. Our magnetic and magnetoresistance measurements show the presence of de Haas–van Alphen (dHvA) and Shubnikov–de Haas (SdH) oscillations. Analysis of these quantum oscillation spectra reveals two major oscillation frequencies (F_α, F_β) with corresponding light effective mass and the nearly π Berry phase for F_α , suggesting the nontrivial band topology in La_3MgBi_5 , which is further supported by our first-principles calculations. Besides, La_3MgBi_5 manifests a large nonsaturating magnetoresistance and a nonlinear Hall effect at low temperatures. Our results show that La_3MgBi_5 is a topological nontrivial material and a member of the A_3MX_5 family exhibiting topological properties, providing a platform for further investigation of topological fermionic properties in this family.

DOI: [10.1103/PhysRevB.108.075157](https://doi.org/10.1103/PhysRevB.108.075157)

I. INTRODUCTION

Topological materials, such as Dirac semimetals and Weyl semimetals, have attracted much attention due to their exotic properties and potential applications. Three-dimensional (3D) Dirac semimetals were predicted and discovered in Na_3Bi and Cd_3As_2 [1–4]. Subsequently, the Weyl semimetals [5–8] and the nodal-line semimetals [9,10] have further expanded the range of topological materials. Up to now, several families of topological material candidates have been extensively investigated, such as the “ LnMPn_2 ” ($\text{Ln} =$ rare earth, Ca-Ba; $M = \text{Mn, Zn}$; $\text{Pn} = \text{Sb, Bi}$) system, “ WHM ” ($W = \text{Zr, Hf}$ or rare earth; $H = \text{Si-Sn, Sb}$; $M = \text{O-Te}$) family, and materials with kagome lattice. Many exotic phenomena has been observed, such as tunable Weyl and Dirac states in CeSbTe [11], quantum Hall effect in bulk antiferromagnet EuMnBi_2 [12], and nontrivial topological electronic structure in the kagome superconductor CsV_3Sb_5 [13,14]. However, many other topological material candidate families remain unexplored, and it is likely that these families could hold great potential for discovering new and intriguing properties that have yet to be uncovered.

The A_3MX_5 family ($A = \text{Ca-Ba}$ or rare earth, $M =$ transition materials or Mg, $X =$ chalcogen or pnictogen) have received considerable attention due to their strong

1D structural characteristic. These materials have shown many interesting magnetic and superconducting phenomena, such as high-pressure-induced superconductivity in Ba_3TiTe_5 [15] and $\text{Ba}_9\text{Fe}_3\text{Te}_{15}$ [16,17], rare ferrotoroidicity with 1D spin chains in $\text{Ba}_6\text{Cr}_2\text{S}_{10}$ [18], and complex magnetism in La_3MnAs_5 [19] and Ce_3TiSb_5 [20]. Recently, $A_3\text{MBi}_5$ compounds have been reported as candidates for topological materials [21]. However, the relevant transport properties of $A_3\text{MBi}_5$ have been rarely explored and the nontrivial topological band has not been experimentally confirmed.

In this work, we have successfully grown single crystals of La_3MgBi_5 and investigated its magnetic and electrical properties. While the crystal structure of La_3MgBi_5 has been confirmed experimentally before, the magnetic and electrical properties of La_3MgBi_5 have not been reported [22]. Our experimental results reveal the presence of de Haas–van Alphen (dHvA) and Shubnikov–de Haas (SdH) oscillations in magnetization and magnetoresistance measurements, respectively. Analysis of these oscillations demonstrates that La_3MgBi_5 has nearly massless relativistic fermions. Besides, our first-principles calculations support the nontrivial band topology in La_3MgBi_5 , confirming that it is a topologically nontrivial material. These findings pave a way for further exploration of topological properties in the A_3MX_5 family.

II. EXPERIMENT DETAILS

Single crystals of La_3MgBi_5 were grown by the flux method. Starting materials of La (ingot, 99.9%, Purui Advanced Material Technology Co. Ltd., Beijing, China), Mg (slug, 99.95%, Alfa Aesar), and Bi (pills, 99.999%,

*These authors contributed equally to this paper.

†Present address: Applied Materials Inc., Santa Clara, CA 95054.

‡Corresponding author: hai.feng@iphy.ac.cn

§Corresponding author: quansheng.wu@iphy.ac.cn

||Corresponding author: ygshe@iphy.ac.cn

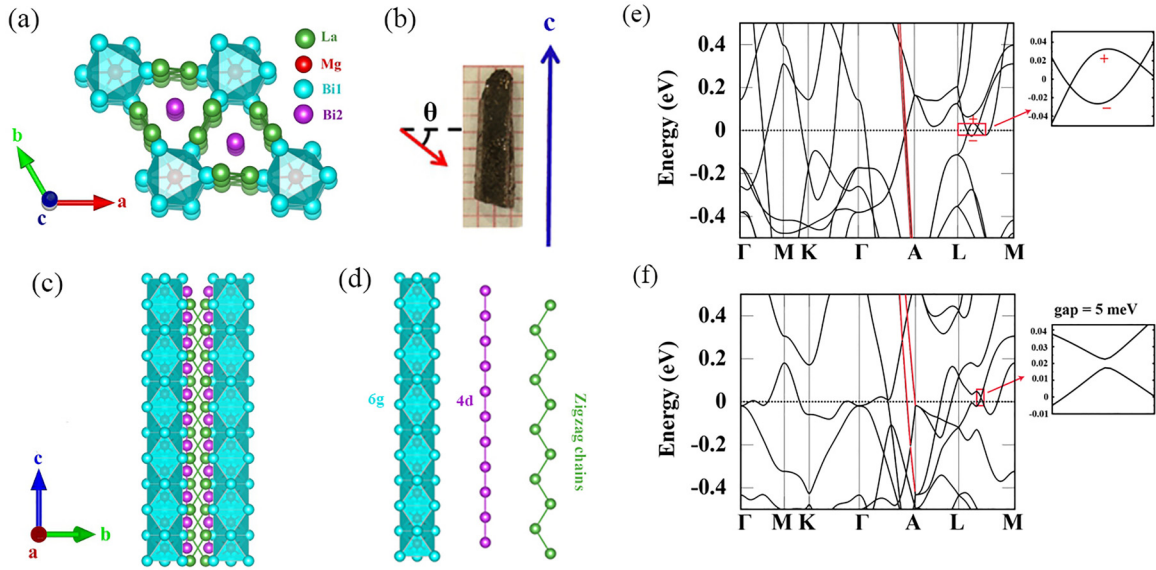


FIG. 1. Structure of La_3MgBi_5 . (a),(c) The schematic crystalline structure of La_3MgBi_5 along c axis and a axis, respectively. (b) A photograph of a typical La_3MgBi_5 single crystal used for dHvA measurement and the schematic configuration for angular (θ) dependent measurement of magnetization (the red square of 1×1 mm indicates the size of the crystal). (d) Three types of 1D motifs in La_3MgBi_5 : The separate 1D MgBi_6 face-sharing octahedral chain, 1D Bi chain, and La zigzag chain. (e),(f) The calculated band structures without and with the consideration of spin-orbit coupling; the red lines are the band projection of the Bi@ $4d$ p_z orbital that exhibits a substantial slope.

Alfa Aesar) with a mole ratio of 1: 4: 6 were mixed and placed into an alumina crucible, which was then sealed in a fully evacuated quartz tube. The tube was heated to 1173 K over 10 h and maintained for 1 d. It was then slowly cooled to 923 K at a rate of 2 K/h followed by centrifuging. Rodlike crystals were obtained, as shown in Fig. 1(b).

Single-crystal x-ray diffraction (XRD) was conducted on a Bruker D8 Venture diffractometer at 274 K using Mo $K\alpha$ radiation ($\lambda = 0.71073 \text{ \AA}$). Crystal structure was refined by the full-matrix least-squares method on F^2 using the SHELXL-2018/3 program. The electrical transport properties were measured in a physical properties measurement system (PPMS, 16 T, Quantum Design) using the standard four-probe technique. Three longer and thinner crystals, SR1, SR2, and SR3, were used for the SdH oscillation measurements. The magnetization measurements were performed on a magnetic property measurement system (MPMS, 7 T, Quantum Design) and the PPMS (9 T, Quantum Design) with a vibrating sample magnetometer (VSM) option. Four different crystals SM1, SM2, SM3, and SM4 were used for the measurement of dHvA oscillations. Each of the crystals is about 40 mg. The specific heat data were measured in the PPMS using its specific heat option with a thermal relaxation method.

III. RESULTS AND DISCUSSION

Analysis of the single-crystal XRD data of La_3MgBi_5 confirms that La_3MgBi_5 has an anti- $\text{Hf}_5\text{Sn}_3\text{Cu}$ hexagonal structure with space group $P6_3/mcm$ (no. 193) which has previously been reported for this compound [22]. This structure belongs to the A_3MX_5 family ($A = \text{Ca-Ba}$ or rare earth, $M =$ transition materials or Mg, $X =$ chalcogen or pnictogen). The refined lattice parameters for La_3MgBi_5 are $a = 9.7792(2) \text{ \AA}$ and $c = 6.5472(2) \text{ \AA}$. The detailed crystallographic data, re-

fining atomic positions, and displacement parameters obtained from the single-crystal XRD data are summarized in Supplemental Material Tables S1, S2, and S3 [23].

Figure 1 depicts the crystal structure of La_3MgBi_5 , which comprises 1D chains of Bi, 1D chains of face-sharing MgBi_6 octahedra, and zigzag chains of La atoms along the c axis. The bismuth atoms in this structure occupy two different Wyckoff positions: the (6g) site for Bi1 and the (4d) site for Bi2. To gain insight into its electronic structure, we performed the first-principles calculations by using the generalized gradient approximation within the Vienna Ab initio Simulation Package (VASP) [24,25]. Figures 1(e) and 1(f) show the band structure calculated with and without spin-orbit coupling (SOC). The band structure in Fig. 1(e) without SOC displays two band crossings near the Fermi level along the L - M direction, forming a nodal ring on the (210) plane that is protected by mirror symmetry. The plus and minus signs indicate the eigenvalue of the mirror symmetry operation. The nodal ring is mainly composed of the p_x and p_y orbitals of Bi atoms in the face-sharing MgBi_6 octahedra. However, when taking the SOC interaction into account, the nodal ring becomes fully gapped. Nonetheless, a small energy gap is observed in the L - M direction [indicated by a red square in Fig. 1(f)], which can be considered a massive Dirac cone with a 5-meV gap and gives rise to the π phase detected in dHvA oscillation. Besides, the band projection of the Bi@ $4d$ p_z orbital between Γ and A exhibits a substantial slope [red line in Figs. 1(e) and 1(f)], indicating a large Fermi velocity and potentially favorable thermal conductivity. Further experiments are needed to explore the thermal properties of La_3MgBi_5 .

Figure 2(a) presents the isothermal magnetization M - B curves at different temperatures measured on SM2 crystal for $B \parallel a$, which exhibits strong dHvA oscillations superimposed on a paramagnetic background [similar dHvA oscillations

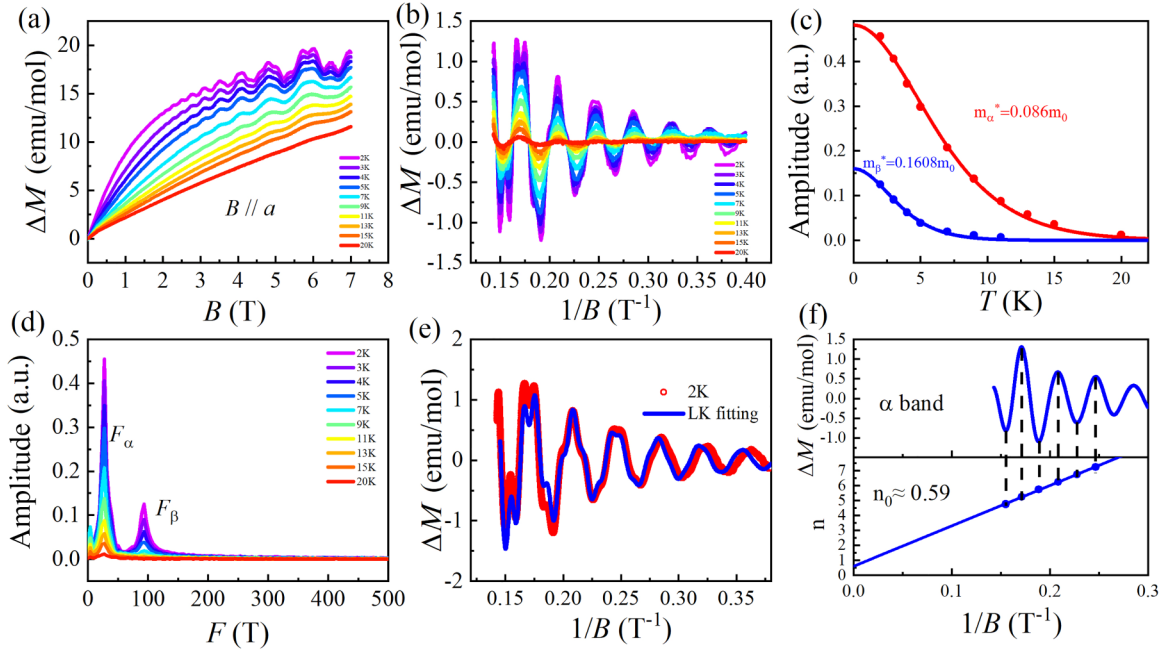


FIG. 2. (a) Isothermal magnetization for La_3MgBi_5 at different temperatures when the magnetic field is parallel to a axis. (b) The oscillatory components of magnetization. (c) The fits of the FFT amplitudes of F_α and F_β to the temperature damping factor R_T by the LK formula. (d) The corresponding FFT spectrum of the oscillatory component of the dHvA oscillations at various temperatures. (e) Multiband LK fit of dHvA oscillations at 2K. (f) The Landau level (LL) index fan diagram for α band derived from the oscillatory magnetization at 2K.

were observed in SM1, SM3, and SM4 (Fig. S3 [23]). In contrast, the M - B curves for $B // c$ show diamagnetic susceptibility without oscillation (Fig. S2 [23]). The oscillations in Fig. 2(a) persist down to a field as low as 2 T at 2 K and can be observed up to 20 K. By subtracting the paramagnetic background, we can extract the oscillatory component of ΔM versus $1/B$ as shown in Fig. 2(b). From the fast Fourier transformation (FFT) analyses of the oscillatory magnetization ΔM , we have derived two oscillation frequencies of 27.29 T (F_α) and 93.58 T (F_β) [Fig. 2(d)]. The F_α component has a much greater oscillation amplitude than the F_β component. Based on the FFT results, we analyzed the extremal cross-sectional area of the FS using the Onsager relation $F = (\Phi_0/2\pi^2) A_F$, where $\Phi_0 = h/2e$ is the magnetic flux quantum. The resulting A_F values are $0.23 \times 10^{-2} \text{ \AA}^{-2}$ for F_α and $0.89 \times 10^{-2} \text{ \AA}^{-2}$ for F_β , respectively.

In general, the dHvA oscillation of a Dirac system can be described by the Lifshitz-Kosevich (LK) formula [26], taking the Berry phase into account [27,28]:

$$\Delta M \propto -B^{1/2} R_T R_D R_S \sin \left[2\pi \left(\frac{F}{B} - \gamma - \delta \right) \right], \quad (1)$$

where $R_T = KT\mu/B/\sinh(KT\mu/B)$, $\mu = m^*/m_e$, $K = 2\pi^2 k_B m_e / (\hbar/e) \approx 14.69 \text{ T/K}$, $R_D = \exp(-KT_D\mu/B)$. T_D is the Dingle temperature and R_S is the spin reduction factor due to Zeeman splitting. The oscillation of ΔM is described by $\sin [2\pi(F/B - \gamma - \delta)]$, in which $\gamma = 1/2 - \varphi_B/2\pi$ and φ_B is the Berry phase. δ is an extra phase factor that depends on the dimensionality of the Fermi surface and takes the value 0 or $\pm 1/8$ for two and three dimensions, respectively, with the sign depending on whether the probed extreme cross-section area of the Fermi surface is maximal or minimal. The fit of the temperature-dependent amplitude to the damping factor

R_T yields $m_\alpha^* = 0.086m_0$ and $m_\beta^* = 0.1608m_0$, as shown in Fig. 2(c). The obtained nearly zero effective mass is comparable with other topological materials such as PtBi_2 [29], PdTe_2 [30], and Cd_3As_2 [31]. To further investigate the relativistic fermions, we fit the oscillation pattern at 2 K by the multiband LK formula with fixed frequency ($F_\alpha = 27.29 \text{ T}$, $F_\beta = 93.58 \text{ T}$) and fixed effective mass ($m_\alpha^* = 0.086m_0$, $m_\beta^* = 0.1608m_0$) [Fig. 2(e)]. The fitted $T_D = 3.455 \text{ K}$ for F_α , and the quantum relaxation time corresponding to the frequency is $\tau_q = \hbar/(2\pi k_B T_D) = 3.52 \times 10^{-13} \text{ s}$, from which the quantum mobility $\mu_q = e\tau_q/m^*$ is estimated to be $7196 \text{ cm}^2/\text{Vs}$ (see Table I). In addition to the light effective mass and high quantum mobility, the Berry phase close to π is another important characteristic of the topological nontrivial band. The LK fit yields a factor $-\gamma - \delta$ of 1.04 for F_α , from which the Berry phase of $(1.54 + \delta) \times 2\pi$ can be derived. Here we take $\delta = 1/8$, since the F_α is a 3D hole pocket as discussed below and the probe F_α oscillation should correspond to a maximal cross section. Thus, the Berry phase is 1.33π , which is close to π and implies a nontrivial Berry phase. The Dingle temperature, relation time, quantum mobility, and Berry phase obtained by LK fitting for F_β are summarized in Table I. Note that δ should be taken as $1/8$ for the F_β corresponding to the minimal cross section of a 3D electron pocket, which will be discussed later.

In addition to the LK fitting, the Berry phase can also be extracted by the Landau level (LL) index fan diagram. Because the DOS (E_F) $\propto dM/dB$ [26], the oscillation peaks of ΔM correspond to the Landau indices of $n + 1/4$, and the oscillation valleys correspond to $n - 1/4$. However, the Landau indices of F_β are far from the quantum limit, resulting in a relatively large uncertainty in determining the intercept. We constructed an LL index fan diagram for the oscillations of

TABLE I. Several characteristic parameters derived from the dHvA and SdH oscillations. Oscillation frequency F ; effective mass m^* ; Dingle temperature T_D ; quantum mobility μ_q ; Berry phase φ_B .

		F (T)	m^*/m_0	T_D (K)	μ_q ($\text{cm}^2 \text{V}^{-1} \text{s}^{-1}$)	φ_B
dHvA	α band	27.29	0.086	3.455	7196	$1.33\pi \pm 0.0014\pi$
($B // a$)	β band	93.58	0.1608	6.44	2056	$1.7596\pi \pm 0.0418\pi$
SdH	α band	31.997	0.108	\	\	$1.3544\pi \pm 0.0344\pi$
($B // ab$)	β band	101.32	0.175	\	\	$1.4364\pi \pm 0.344\pi$ or $0.9364 \pm 0.344\pi$
	η band	391.96	0.245	\	\	\

$F_\alpha = 27.29$ T, as shown in Fig. 2(f). The slope of the linear fit of the LL indices is 27.03 T, which is nearly the same as the value obtained from FFT (27.29 T), indicating the reliability of linear fit in the LL fan diagram. The intercept derived from the linear extrapolation is (0.59 ± 0.009024) , corresponding to a Berry phase of $1.43\pi \pm 0.018\pi$ which is consistent with the result obtained from LK fitting. However, it should be noted that a finite Berry phase deviating from the exact value of π can also occur as a result of the deviation from an ideal linear dispersion [32]. In this material, the presence of the SOC gives rise to a narrow energy gap at the Dirac point, leading to the berry phase that slightly deviates from π .

To investigate the anisotropy of the electronic structure of La_3MgBi_5 , we performed the dHvA experiments with the magnetic field being rotated from $B // a$ to $B // c$ at 2 K [Fig. 3(a)]. The magnetization gradually changes from paramagnetic to diamagnetic with the θ increasing from 0° to 90° [Fig. 3(a)]. After subtracting a smooth background, we obtained the oscillation pattern of ΔM versus $1/B$ curves at various angles, which was gradually suppressed with the increasing θ and became nonobservable when θ reached 49° , as shown in Fig. 3(b). From the FFT analyses [Fig. 3(c)], we determined the angular dependence of the oscillation frequencies. A new frequency $F_{\alpha'}$ emerged with the increasing the angle [see Fig. 3(c)]. The angular dependence of oscillation frequencies [Fig. 3(d)] suggests complicated Fermi surfaces, which is confirmed by our first-principles calculations.

In addition to the dHvA oscillations, we conducted transport measurements on La_3MgBi_5 to obtain further information associated with the relativistic fermions. As depicted in Fig. 4(a), temperature-dependent resistivities indicate metallic behavior for both $I // c$ (ρ_{xx}) and $I // ab$ (ρ_{zz}). The residual resistivity ratio (RRR) defined as $\rho(300 \text{ K})/\rho(2 \text{ K})$ is 36 for ρ_{xx} . The ρ_{zz}/ρ_{xx} ratio increases with decreasing temperature and reaches approximately 20 at 2 K [inset to Fig. 4(a)], which reflects the anisotropic Fermi surface in La_3MgBi_5 . Figure 4(b) shows the temperature dependence of the ρ_{xx} measured under zero fields, 9 and 16 T. A positive magnetoresistance (MR) is observed at lower temperatures. For $B = 16$ T, the ρ_{xx} curve shows a minimum at around 25 K and slightly increases below 25 K. Similar behaviors have also been observed in other topological materials such as TaP [33], NbP [34], WTe_2 [6] and TaAs [35], which were explained with the Kohler's rule [36]. Figure 4(c) presents the field dependence of $\rho_{xx}(B)$ up to 16 T measured in SR2 at various temperatures. La_3MgBi_5 exhibits a large positive MR without saturation (+600%) at $T = 2$ K [inset of Fig. 4(c)]. Figure 4(f) shows the numerical simulations for the magnetic field dependence of MR. The calculated $\rho_{xx}^* \tau$ shows a nonsaturating $(B\tau)^{1.5}$ dependence when $B // ab$, which is quite consistent with the experimental results of $\text{MR} \propto B^{1.55}$. The magnetoresistance shown in Fig. 4(f) was calculated using the WANNIERTOOLS package [37] based on the Boltzmann transport equation [38,39] and the Wannier function techniques [40]. The calculation was carried out on

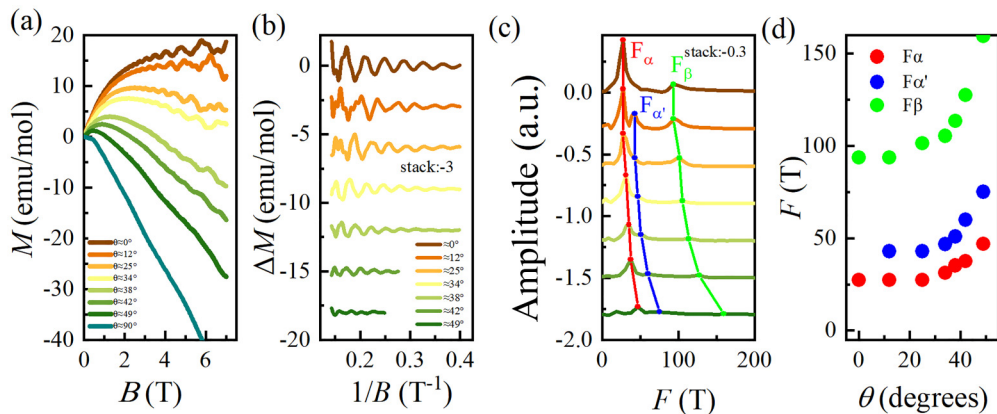


FIG. 3. (a) Isothermal magnetization of La_3MgBi_5 at different angles for $T = 2$ K. (b) The oscillatory components of magnetization at 2 K under different magnetic field orientations. (c) The corresponding FFT spectrum of the oscillatory component of the dHvA oscillations at various angles. (d) The angular dependence of dHvA oscillation frequencies $F_\alpha, F_{\alpha'}, F_\beta$.

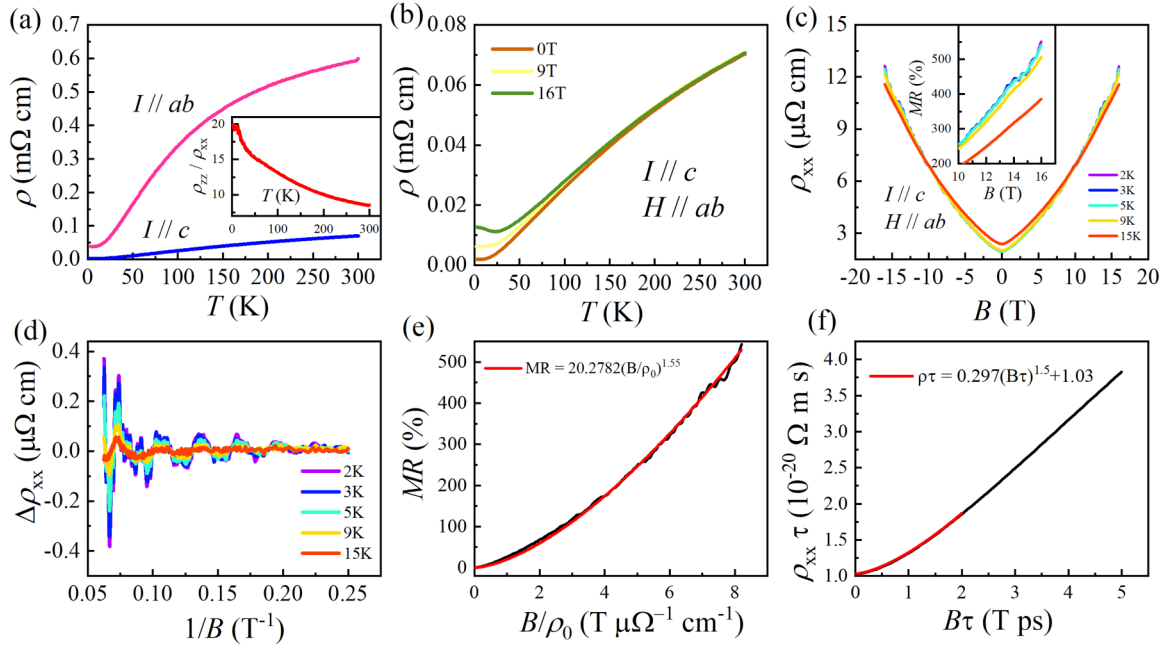


FIG. 4. (a) Temperature dependence of resistivity ρ_{xx} ($I//c$) and ρ_{zz} ($I//ab$ plane). Inset: Temperature dependence of the ratio of ρ_{zz}/ρ_{xx} . (b) Temperature dependence of $\rho_{xx}(T)$ with various fields. (c) Field dependence of $\rho_{xx}(B)$ at various temperatures. The inset shows an enlarged view of the MR above 10 T. (d) The oscillatory components of magnetoresistance. (e),(f) Black lines show the measured (e) and the calculated (f) MR at 2 K as a function of the magnetic field. Red lines are the fitting data as a power function of the magnetic field.

a $51 \times 51 \times 51 k$ mesh and the charge carriers are assumed to have the same relaxation time τ . The agreement between calculation and experiment indicates that the MR can be fully explained by the semiclassical theory while the topological properties, such as the massive Dirac point, have no contribution.

In the high-field range, the $\rho_{xx}(B)$ curves show the SdH oscillations which decay with increasing temperatures. (This phenomenon is also reproduced for samples SR1 and SR3, as shown in Supplemental Material Fig. S4 [23].) However, compared with the strong dHvA oscillations, the SdH oscillations of La_3MgBi_5 are relatively weak. It could be attributed to a strong background in MR, as has been discussed in PdTe_2 [30] and BaZnBi_2 [41]. After subtracting a smooth background, the oscillatory parts $\Delta\rho_{xx}$ as a function of $1/B$ is shown in Fig. 4(d). The FFT of the SdH oscillations yields three major frequencies, $F_\alpha = 31.997$ T, $F_\beta = 101.32$ T, $F_\eta = 391.96$ T, and a harmonic frequency of $2F_\alpha$ [Fig. 5(a)]. The frequency of F_α and F_β are close to the results measured by the dHvA oscillations. However, the F_η was not detected in the dHvA results, possibly due to the wider range of magnetic fields applied for MR measurement. Similarly, we obtained the effect mass $m_\alpha^* = 0.108m_0$, $m_\beta^* = 0.175m_0$, and $m_\eta^* = 0.247m_0$ by fitting the temperature dependence of the FFT amplitudes to R_T [inset to Fig. 5(a)]. The F_α , F_β , m_α^* , and m_β^* obtained from the SdH oscillations are slightly larger than those from dHvA oscillations. One of the reasons is that SdH oscillations are affected by the scattering mechanism, thus deviating from the prediction by the LK theory. However, the dHvA oscillation is not impacted by the scattering mechanism and can be well interpreted by LK theory [10,29,42,43].

In SdH oscillations, the oscillatory part of the conductivity follows $\sigma_{xx} \propto \cos[2\pi(F/B - \gamma)]$, where $\gamma = 1/2 - \varphi_B/2\pi$.

The minima of the oscillations in σ_{xx} are assigned to the Landau indices n while the Berry phases φ_B can be determined from analysis of the LL fan diagram [26]. Since the σ_{xx} can be obtained from the longitudinal resistivity ρ_{xx} and the Hall resistivity ρ_{yx} using $\sigma_{xx} = \rho_{xx}/(\rho_{xx}^2 + \rho_{yx}^2)$, the minima of ρ_{xx} is used for indexing the integer n when $\rho_{xx} \ll \rho_{yx}$ and the maxima of ρ_{xx} is used for indexing the integer n when $\rho_{xx} \gg \rho_{yx}$.

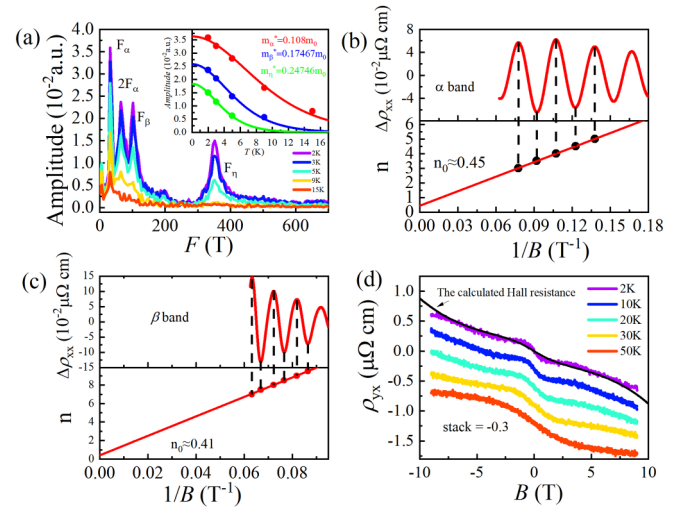


FIG. 5. (a) The corresponding FFT spectrum of the oscillatory component of the SdH oscillations at various temperatures. Inset: The fits of the FFT amplitudes of F_α , F_β , and F_η to the temperature damping factor R_T . (b),(c) The Landau level (LL) index fan diagram for α band and β band derived from the SdH oscillations at 2 K, respectively. (d) Field dependence of Hall resistivity $\rho_{yx}(B)$ at several different temperatures; the black line is the calculated Hall resistance.

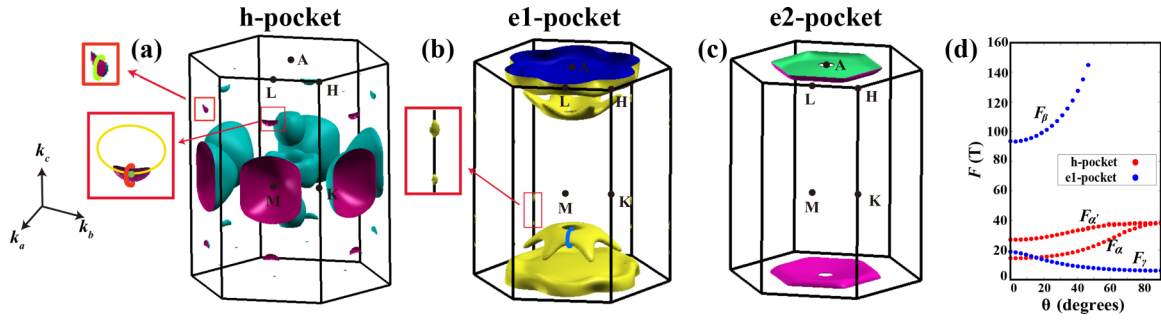


FIG. 6. (a)–(c) The Fermi surfaces with SOC included. (a) The hole pocket referred as *h* pocket. The red box shows the enlarged pocket, where the green line in the upper box and the red line in the lower box indicate the extreme orbit of $F_{\alpha'}$ and F_{α} , respectively. The yellow line and green spot indicate the nodal ring without SOC and massive Dirac point with SOC, respectively. (b) The electron pockets referred as *e1* pocket with the red box showing the enlarged pocket in the *H*-*K* direction. The blue line on the hexagonal hollow pocket shows the extreme orbit of F_{β} ($\theta = 0^\circ$). (c) The electron pocket referred as *e2* pocket. (d) The angular dependence of calculated dHvA oscillation frequencies below 160 T. F_{α} , $F_{\alpha'}$ contributed from *h* pocket are denoted with red spots while F_{β} , F_{γ} contributed from *e1* pocket are denoted with blue spots.

[44]. In our study, the ρ_{xx} is about ten times larger than ρ_{xy} at 2K, indicating that $\rho_{xx} \approx 1/\sigma_{xx}$ and the Landau indices of n should be assigned to maxima in $\Delta\rho_{xx}$. Figures 5(b) and 5(c) show the LL fan diagram for F_{α} and F_{β} , respectively. The intercept obtained from the extrapolation of the linear fit in the fan diagram is 0.4478 ± 0.01734 for F_{α} and 0.4068 ± 0.172 for F_{β} . In SdH oscillation measurements, the direction of the magnetic field in the *ab* plane is uncertain because the samples are very thin. Consequently, the extremal orbit of the electron pocket corresponding to F_{β} can be either maximal or minimal, depending on the magnetic field direction. This uncertainty leads to δ being either $+1/8$ or $-1/8$ for F_{β} , resulting in an uncertain phase of $1.4364\pi \pm 0.344\pi$ or $0.9364\pi \pm 0.344\pi$ for F_{β} . In contrast, the extremal orbit of the F_{α} pocket always corresponds to a maximal cross section as the magnetic field changes in the *ab* plane. Therefore, for F_{α} , we have $\varphi_B = 1.3544\pi \pm 0.0344\pi$ [14]. Moreover, the fitted oscillation frequency is 33.14 T for F_{α} and 105.265 T for F_{β} , which are close to the results from the FFT, indicating the reliability of linear fit in the LL fan diagram. The result for F_{α} is consistent with dHvA oscillations indicating a nontrivial Berry phase. However, the large fitting errors and undetermined field directions prevent us from obtaining a relatively accurate φ_B for F_{β} . Furthermore, the lowest Landau index for F_{η} is also far from the quantum limit, making it challenging to determine its intercept with certainty.

The Hall resistivity ρ_{yx} of La_3MgBi_5 , as shown in Fig. 5(d), exhibits nonlinear behavior up to 200 K (Fig. S5 [23]), suggesting the presence of multiple kinds of carriers with different densities and mobilities. To calculate the carrier densities and mobilities of La_3MgBi_5 , we used a three-band model [45,46],

$$\sigma_{xx}(B) = e \left(\frac{n_1\mu_1}{1+\mu_1^2B^2} + \frac{n_2\mu_2}{1+\mu_2^2B^2} + \frac{n_3\mu_3}{1+\mu_3^2B^2} \right), \quad (2)$$

$$\sigma_{xy}(B) = eB \left(\frac{n_1\mu_1^2}{1+\mu_1^2B^2} + \frac{n_2\mu_2^2}{1+\mu_2^2B^2} + \frac{n_3\mu_3^2}{1+\mu_3^2B^2} \right), \quad (3)$$

to fit the conductivity σ_{xx} and Hall conductivity $\sigma_{xy} = \rho_{yx}/(\rho_{xx}^2 + \rho_{yy}^2)$ at $T = 2$ K. (The fitting results are shown in Supplemental Material Fig. S7 [23].) The fitting

indicates that the carrier densities of La_3MgBi_5 are $n_{e1} = 1.14 \times 10^{21}\text{cm}^{-3}$, $n_{e2} = 1.9 \times 10^{20}\text{cm}^{-3}$, and $n_h = 6.55 \times 10^{20}\text{cm}^{-3}$ at 2 K. The carrier mobilities obtained from the fitting are $\mu_{e1} = 897\text{cm}^2\text{V}^{-1}\text{s}^{-1}$, $\mu_{e2} = 4743\text{cm}^2\text{V}^{-1}\text{s}^{-1}$, and $\mu_h = 1843\text{cm}^2\text{V}^{-1}\text{s}^{-1}$. It should be pointed out that the three-band model cannot precisely describe the conductivity and Hall resistivity of La_3MgBi_5 . However, if all bands are considered, it would be difficult to obtain meaningful information due to a large number of fitting parameters. Additionally, the Hall resistivity is calculated using the Boltzmann transport equation [38,39] and the Wannier function technique [37], based on first-principles calculations. The resulting simulated Hall resistivity curve is depicted as the black line in Fig. 5(d), considering a relaxation time of 0.25 ps. Remarkably, this simulation aligns well with the experimental measurements, demonstrating multicarrier behavior.

Figures 6(a)–6(c) depict the Fermi surfaces with SOC, comprising one hole pocket (*h* pocket) and two electron pockets (*e1* pocket and *e2* pocket). The inset of Fig. 6(a) shows the location of the nodal ring and massive Dirac cone, denoted by a yellow circle and green spot, respectively. Using the SKEAF package [47], we calculated the angular dependence of dHvA oscillation frequencies, which are shown in Fig. 6(d) and exhibit good agreement with experimental results. Note that we only display dHvA oscillation frequencies below 160 T as detecting higher frequencies in experiments necessitates a stronger magnetic field, lower temperature, and cleaner sample.

Assisted by the calculations, we can determine the origin of the dHvA frequencies detected in experiments. The F_{β} frequency is contributed by the extremal orbit on the hexagonal hollow pockets in Fig. 6(b), with the extremal orbit of F_{β} ($\theta = 0^\circ$) indicated by a blue line. The electron pockets in the *K*-*H* direction [enlarged in the red box in Fig. 6(b)] contribute to F_{γ} . The smaller hole pockets in the *L*-*M* direction shown in Fig. 6(a) give rise to the F_{α} and $F_{\alpha'}$ frequencies. The hole pockets can be classified into two types based on the angle between their located plane and the magnetic field when $\theta < 90^\circ$. Consequently, $F_{\alpha}(\theta < 90^\circ)$ is different from ($\theta < 90^\circ$) before θ increases to 90° . Moreover, the extremal orbit of $F_{\alpha/\alpha'}(\theta = 0^\circ)$ wraps around the massive Dirac point

and then deviates from the point with increasing θ , resulting in the decreasing amplitude of $F_{\alpha/\alpha'}$, as shown in Fig. 3(c).

IV. CONCLUSIONS

We have successfully grown high-quality single crystals of La_3MgBi_5 , a member of the A_3MX_5 family, and performed systematic measurements for magnetization and electrical transport properties. Our results show that La_3MgBi_5 has anisotropic magnetic susceptibility and displays the dHvA oscillations in the case of $B \parallel a$. Analysis of the oscillation patterns reveals high quantum mobilities, light effective masses, and nontrivial Berry phase for the relativistic fermions. Additionally, La_3MgBi_5 shows large positive MR without saturation and the SdH oscillations. The nontrivial Berry phase can also be obtained by SdH oscillations. Large nonsaturating magnetoresistance can be explained by the Boltzmann transport model. Furthermore, the nonlinear Hall effect at low temperature indicates that La_3MgBi_5 is a multiband system. Our experimental results agree with the first-principles calculations, indicating that La_3MgBi_5 is an interesting material

for observing topological phases. Moreover, as La_3MgBi_5 is a member of the extensive A_3MX_5 family, our research may inspire further investigations into magnetic compounds (when $A =$ magnetic rare earth elements or $M =$ magnetic transition metals) within this family. If such compounds also exhibit relativistic fermions, they could present exciting opportunities to explore the intricate interplay between complex magnetism and relativistic fermions.

ACKNOWLEDGMENTS

We thank G. Li, Y. Ma, and M. Yang for valuable discussions. This work was supported by the National Key Research and Development Program of China (Grant No. 2021YFA1400401), the National Natural Science Foundation of China (Grants No. U2032204, No. 12274436, No. 12188101, No. U22A6005, and No. 12104492), the Strategic Priority Research Program of the Chinese Academy of Sciences (Grant No. XDB33010000), the Informatization Plan of Chinese Academy of Sciences (Grant No. CAS-WX2021SF-0102), and the China Postdoctoral Science Foundation (Grant No. 2021TQ0356).

-
- [1] T. Liang, Q. Gibson, M. N. Ali, M. Liu, R. J. Cava, and N. P. Ong, Ultrahigh mobility and giant magnetoresistance in the dirac semimetal Cd_3As_2 , *Nat. Mater.* **14**, 280 (2015).
- [2] Z. K. Liu, J. Jiang, B. Zhou, Z. J. Wang, Y. Zhang, H. M. Weng, D. Prabhakaran, S.-K. Mo, H. Peng, P. Dudin *et al.*, A stable three-dimensional topological dirac semimetal Cd_3As_2 , *Nat. Mater.* **13**, 677 (2014).
- [3] Z. K. Liu, B. Zhou, Y. Zhang, Z. J. Wang, H. M. Weng, D. Prabhakaran, S.-K. Mo, Z. X. Shen, Z. Fang, X. Dai *et al.*, Discovery of a three-dimensional topological dirac semimetal, Na_3Bi , *Science* **343**, 864 (2014).
- [4] Z. Wang, Y. Sun, X.-Q. Chen, C. Franchini, G. Xu, H. Weng, X. Dai, and Z. Fang, Dirac semimetal and topological phase transitions in $A_3\text{Bi}$ ($A = \text{Na}, \text{K}, \text{Rb}$), *Phys. Rev. B* **85**, 195320 (2012).
- [5] B. Q. Lv, H. M. Weng, B. B. Fu, X. P. Wang, H. Miao, J. Ma, P. Richard, X. C. Huang, L. X. Zhao, G. F. Chen *et al.*, Experimental Discovery of Weyl Semimetal TaAs , *Phys. Rev. X* **5**, 031013 (2015).
- [6] M. N. Ali, J. Xiong, S. Flynn, J. Tao, Q. D. Gibson, L. M. Schoop, T. Liang, N. Haldolaarachchige, M. Hirschberger, N. P. Ong *et al.*, Large, non-saturating magnetoresistance in WTe_2 , *Nature (London)* **514**, 205 (2014).
- [7] N. Morali, R. Batabyal, P. K. Nag, E. Liu, Q. Xu, Y. Sun, B. Yan, C. Felser, N. Avraham, and H. Beidenkopf, Fermi-Arc diversity on surface terminations of the magnetic weyl semimetal $\text{Co}_3\text{Sn}_2\text{S}_2$, *Science* **365**, 1286 (2019).
- [8] C. Liu, J. Shen, J. Gao, C. Yi, D. Liu, T. Xie, L. Yang, S. Danilkin, G. Deng, W. Wang *et al.*, Spin excitations and spin wave gap in the ferromagnetic weyl semimetal $\text{Co}_3\text{Sn}_2\text{S}_2$, *Sci. China Phys. Mech. Astron.* **64**, 217062 (2021).
- [9] L. M. Schoop, M. N. Ali, C. Straßer, A. Topp, A. Varykhalov, D. Marchenko, V. Duppel, S. S. P. Parkin, B. V. Lotsch, and C. R. Ast, Dirac cone protected by non-symmorphic symmetry and three-dimensional dirac line node in ZrSiS , *Nat. Commun.* **7**, 11696 (2016).
- [10] J. Hu, Z. Tang, J. Liu, Y. Zhu, J. Wei, and Z. Mao, Nearly massless dirac fermions and strong zeeman splitting in the nodal-line semimetal ZrSiS probed by de Haas-van Alphen quantum oscillations, *Phys. Rev. B* **96**, 045127 (2017).
- [11] L. M. Schoop, A. Topp, J. Lippmann, F. Orlandi, L. Muehler, M. G. Vergniory, Y. Sun, A. W. Rost, V. Duppel, M. Krivenkov *et al.*, Tunable weyl and dirac states in the nonsymmorphic compound CeSbTe , *Sci. Adv.* **4**, eaar2317 (2018).
- [12] H. Masuda, H. Sakai, M. Tokunaga, Y. Yamasaki, A. Miyake, J. Shiogai, S. Nakamura, S. Awaji, A. Tsukazaki, H. Nakao *et al.*, Quantum hall effect in a bulk antiferromagnet EuMnBi_2 with magnetically confined two-dimensional dirac fermions, *Sci. Adv.* **2**, e1501117 (2016).
- [13] Y. Hu, S. M. L. Teicher, B. R. Ortiz, Y. Luo, S. Peng, L. Huai, J. Ma, N. C. Plumb, S. D. Wilson, J. He *et al.*, Topological surface states and flat bands in the kagome superconductor CsV_3Sb_5 , *Sci. Bull.* **67**, 495 (2022).
- [14] Y. Fu, N. Zhao, Z. Chen, Q. Yin, Z. Tu, C. Gong, C. Xi, X. Zhu, Y. Sun, K. Liu *et al.*, Quantum Transport Evidence of Topological Band Structures of Kagome Superconductor CsV_3Sb_5 , *Phys. Rev. Lett.* **127**, 207002 (2021).
- [15] J. Zhang, Y. Jia, X. Wang, Z. Li, L. Duan, W. Li, J. Zhao, L. Cao, G. Dai, Z. Deng *et al.*, A new quasi-one-dimensional compound Ba_3TiTe_5 and superconductivity induced by pressure, *NPG Asia Mater.* **11**, 60 (2019).
- [16] J. Zhang, L. Duan, Z. Wang, X. Wang, J. Zhao, M. Jin, W. Li, C. Zhang, L. Cao, Z. Deng *et al.*, The synthesis of a quasi-one-dimensional iron-based telluride with antiferromagnetic chains and a spin glass state, *Inorg. Chem.* **59**, 5377 (2020).
- [17] J. Zhang, M.-L. Jin, X. Li, X.-C. Wang, J.-F. Zhao, Y. Liu, L. Duan, W.-M. Li, L.-P. Cao, B.-J. Chen *et al.*, Structure-spin-transport anomaly in quasi-one-dimensional $\text{Ba}_9\text{Fe}_3\text{Te}_{15}$ under high pressure, *Chin. Phys. Lett.* **37**, 087106 (2020).

- [18] J. Zhang, X. Wang, L. Zhou, G. Liu, D. T. Adroja, I. da Silva, F. Demmel, D. Khalyavin, J. Sannigrahi, H. S. Nair *et al.*, A ferrotoroidic candidate with well-separated spin chains, *Adv. Mater.* **34**, 2106728 (2022).
- [19] L. Duan, X. C. Wang, J. Zhang, Z. Hu, J. F. Zhao, Y. G. Feng, H. L. Zhang, H.-J. Lin, C. T. Chen, W. Wu *et al.*, Synthesis, structure, and magnetism in the ferromagnet La_3MnAs_5 : Well-separated spin chains coupled via itinerant electrons, *Phys. Rev. B* **106**, 184405 (2022).
- [20] C. Ritter, A. K. Pathak, R. Filippone, A. Provino, S. K. Dhar, and P. Manfrinetti, Magnetic ground states of Ce_3TiSb_5 , Pr_3TiSb_5 and Nd_3TiSb_5 determined by neutron powder diffraction and magnetic measurements, *J. Phys.: Condens. Matter* **33**, 245801 (2021).
- [21] J. F. Khoury, B. Han, M. Jovanovic, R. Singha, X. Song, R. Queiroz, N.-P. Ong, and L. M. Schoop, A class of Magnetic Topological Material Candidates with Hypervalent Bi Chains, *J. Am. Chem. Soc.* **144**, 9785 (2022).
- [22] D.-C. Pan, Z.-M. Sun, and J.-G. Mao, Synthesis and crystal structures of La_3MgBi_5 and LaLiBi_2 , *J. Solid State Chem.* **179**, 1016 (2006).
- [23] See Supplemental Material at <http://link.aps.org/supplemental/10.1103/PhysRevB.108.075157> for details of crystal structure and transport properties.
- [24] G. Kresse and J. Furthmüller, Efficient iterative schemes for ab initio total-energy calculations using a plane-wave basis set, *Phys. Rev. B* **54**, 11169 (1996).
- [25] G. Kresse and D. Joubert, From ultrasoft pseudopotentials to the projector augmented-wave method *Phys. Rev. B* **59**, 1758 (1999).
- [26] D. Shoenberg, *Magnetic Oscillations in Metals* (Cambridge University Press, Cambridge, UK, 1984).
- [27] J. Hu, Z. Tang, J. Liu, X. Liu, Y. Zhu, D. Graf, K. Myhro, S. Tran, C. N. Lau, J. Wei *et al.*, Evidence of Topological Nodal-Line Fermions in ZrSiSe and ZrSiTe , *Phys. Rev. Lett.* **117**, 016602 (2016).
- [28] G. P. Mikitik and Yu. V. Sharlai, Manifestation of Berry's Phase in Metal Physics, *Phys. Rev. Lett.* **82**, 2147 (1999).
- [29] W. Gao, X. Zhu, J. Hu, S. Li, F. Zheng, H. Zhang, M. Wu, G. Zheng, N. Hao, P. Zhang *et al.*, De Haas-van alphen study on three-dimensional topological semimetal pyrite PtBi_2 , *Sci. Bull.* **64**, 1496 (2019).
- [30] F. Fei, X. Bo, R. Wang, B. Wu, J. Jiang, D. Fu, M. Gao, H. Zheng, Y. Chen, X. Wang *et al.*, Nontrivial berry phase and type-II dirac transport in the layered material PdTe_2 , *Phys. Rev. B* **96**, 041201 (2017).
- [31] L. P. He, X. C. Hong, J. K. Dong, J. Pan, Z. Zhang, J. Zhang, and S. Y. Li, Quantum Transport Evidence for the Three-Dimensional Dirac Semimetal Phase in Cd_3As_2 , *Phys. Rev. Lett.* **113**, 246402 (2014).
- [32] A. A. Taskin and Y. Ando, Berry phase of nonideal dirac fermions in topological insulators, *Phys. Rev. B* **84**, 035301 (2011).
- [33] J. Hu, J. Y. Liu, D. Graf, S. M. A. Radmanesh, D. J. Adams, A. Chuang, Y. Wang, I. Chiorescu, J. Wei, L. Spinu *et al.*, π Berry phase and zeeman splitting of weyl semimetal tap, *Sci. Rep.* **6**, 18674 (2016).
- [34] C. Shekhar, A. K. Nayak, Y. Sun, M. Schmidt, M. Nicklas, I. Leermakers, U. Zeitler, Y. Skourski, J. Wosnitza, Z. Liu *et al.*, Extremely large magnetoresistance and ultrahigh mobility in the topological weyl semimetal candidate NbP , *Nat. Phys.* **11**, 645 (2015).
- [35] X. Huang, L. Zhao, Y. Long, P. Wang, D. Chen, Z. Yang, H. Liang, M. Xue, H. Weng, Z. Fang *et al.*, Observation of the Chiral-Anomaly-Induced Negative Magnetoresistance in 3d Weyl Semimetal TaAs , *Phys. Rev. X* **5**, 031023 (2015).
- [36] Y. L. Wang, L. R. Thoutam, Z. L. Xiao, J. Hu, S. Das, Z. Q. Mao, J. Wei, R. Divan, A. Luican-Mayer, G. W. Crabtree *et al.*, Origin of the turn-on temperature behavior in WTe_2 , *Phys. Rev. B* **92**, 180402 (2015).
- [37] Q. Wu, S. Zhang, H.-F. Song, M. Troyer, and A. A. Soluyanov, WannierTools: An open-source software package for novel topological materials, *Comput. Phys. Commun.* **224**, 405 (2018).
- [38] S. Zhang, Q. Wu, Y. Liu, and O. V. Yazyev, Magnetoresistance from fermi surface topology, *Phys. Rev. B* **99**, 035142 (2019).
- [39] Y. Liu, H.-J. Zhang, and Y. Yao, *Ab initio* investigation of magnetic transport properties by Wannier interpolation, *Phys. Rev. B* **79**, 245123 (2009).
- [40] A. A. Mostofi, J. R. Yates, Y.-S. Lee, I. Souza, D. Vanderbilt, and N. Marzari, Wannier90: A tool for obtaining maximally-localised Wannier functions, *Comput. Phys. Commun.* **178**, 685 (2008).
- [41] K. Zhao, E. Golias, Q. H. Zhang, M. Krivenkov, A. Jesche, L. Gu, O. Rader, I. I. Mazin, and P. Gegenwart, Quantum oscillations and dirac dispersion in the BaZnBi_2 semimetal guaranteed by local Zn vacancy order, *Phys. Rev. B* **97**, 115166 (2018).
- [42] J. Y. Liu, J. Hu, Q. Zhang, D. Graf, H. B. Cao, S. M. A. Radmanesh, D. J. Adams, Y. L. Zhu, G. F. Cheng, X. Liu *et al.*, A Magnetic Topological Semimetal $\text{Sr}_{1-y}\text{Mn}_{1-z}\text{Sb}_2$ ($y, z < 0.1$), *Nat. Mater.* **16**, 905 (2017).
- [43] L. An, X. Zhu, Y. Qian, C. Xi, W. Ning, H. Weng, and M. Tian, Signature of Dirac semimetal states in gray arsenic studied by de Haas-van Alphen and Shubnikov-de Haas quantum oscillations, *Phys. Rev. B* **101**, 205109 (2020).
- [44] F.-X. Xiang, X.-L. Wang, M. Veldhorst, S.-X. Dou, and M. S. Fuhrer, Observation of topological transition of fermi surface from a spindle torus to a torus in bulk rashba spin-split BiTeCl , *Phys. Rev. B* **92**, 035123 (2015).
- [45] K. Akiba, A. Miyake, Y. Akahama, K. Matsubayashi, Y. Uwatoko, and M. Tokunaga, Two-carrier analyses of the transport properties of black phosphorus under pressure, *Phys. Rev. B* **95**, 115126 (2017).
- [46] D. E. Soule, Magnetic field dependence of the hall effect and magnetoresistance in graphite single crystals, *Phys. Rev.* **112**, 698 (1958).
- [47] P. M. C. Rourke and S. R. Julian, Numerical extraction of de Haas-van Alphen frequencies from calculated band energies, *Comput. Phys. Commun.* **183**, 324 (2012).